Fe/Sb_2Te_3 interface reconstruction through mild thermal annealing

Emanuele Longo, Claudia Wiemer, Raimondo Cecchini, Massimo Longo, Alessio Lamperti, Anton Khanas, Andrei Zenkevich, Matteo Cantoni, Christian Rinaldi, Marco Fanciulli and Roberto Mantovan**

Emanuele Longo*, Dr. Claudia Wiemer, Dr. Raimondo Cecchini, Dr. Massimo Longo, Dr. Alessio Lamperti, Dr. Roberto Mantovan*
CNR-IMM, Unit of Agrate Brianza, Via C. Olivetti 2, 20864, Agrate Brianza (MB), Italy,
E-mail: emanuele.longo@mdm.imm.cnr.it
E-mail: roberto.mantovan@mdm.imm.cnr.it

Emanuele Longo, Prof. Marco Fanciulli
Università degli Studi di Milano-Bicocca, Dipartimento di Scienze dei Materiali, Via R. Cozzi 55, 20126, Milano, Italy,

Dr. Anton Khanas, Dr. Andrei Zenkevich
Moscow Institute of Physics and Technology, Dolgoprudny, Moscow region 141701, Russian Federation.

Prof. Matteo Cantoni, Dr. Christian Rinaldi
Dipartimento di Fisica, Politecnico di Milano, Via G. Colombo 81, 20131 Milano, Italy

Keywords: Topological Insulators, Ferromagnetism, Spintronics.

"This is the pre-peer reviewed version of the following article: "Fe/Sb_2Te_3 Interface Reconstruction through Mild Thermal Annealing by E. Longo et al., which has been published in final form at Advanced Material Interfaces (2020): https://onlinelibrary.wiley.com/doi/abs/10.1002/admi.202000905. This article may be used for non-commercial purposes in accordance with Wiley Terms and Conditions for Use of Self-Archived Versions."

Abstract

When coupled with ferromagnetic (FM) layers, topological insulators (TI) are expected to boost the charge-to-spin conversion efficiency across the FM/TI interface. In this context, a thorough control and optimization of the FM/TI interface quality are requested. In this paper, the evolution of the chemical, structural, and magnetic properties of the Fe/Sb_2Te_3 heterostructure, as a function of a rapid mild (up to 200 °C) thermal annealing conducted on the Sb_2Te_3-TI only, is presented. The annealing of Sb_2Te_3 markedly improves its crystalline quality, leading to an increased fraction of ferromagnetic Fe atoms at the buried Fe/Sb_2Te_3 interface and a slight lowering of the Fe layer coercive field. This is quite surprising, since the bi-layer is not subjected to any thermal treatment upon Fe deposition. This method is an efficient tool to clean-up the Fe/Sb_2Te_3 interface, which may be extended to different FM/TI heterostructures. Simultaneously to the interface reconstruction, a constant ∼20% fraction of FeTe develops at the interface. Since ultrathin FeTe has been reported to be superconducting, these results can open perspective in exploiting phenomena at the edge of magnetism, superconductivity and topology.

1. Introduction

Topological insulators (TI) are gaining attention in the context of spintronics, mainly as ideal candidates to replace heavy metals (Pt, Ta, etc.) at the interface with ferromagnetic (FM) layers, in order to exploit optimized spin-to-charge conversion effects [1–4].

However, there are several open questions. First, since the role played by the specific chemical bonds and/or the presence of magnetically dead-layers in affecting the spin-to-charge conversion efficiency is not completely understood, it is necessary to investigate and optimize the chemical, structural and magnetic properties of the FM/TI interfaces [2,5]. Moreover, from the technological point of view, the growth of FM layers is usually conducted in a separate vacuum process than that used for the synthesis of TIs. Therefore, in order to protect the TI surface during the transfer, *in situ* capping is often adopted [6], which subsequently requires a critical process of its full removal before the FM deposition. Another option is to introduce an ultrathin interlayer between the FM and TI, but the trade-off between benefits and criticalities is still under debate.

We propose an alternative method to prepare the TI surface, consisting of a mild Rapid Thermal Annealing (RTA) process prior to the FM deposition. In particular, our focus is the interface between Fe and the 3D-TI Sb_2Te_3 produced by Metal Organic Chemical Vapor Deposition (MOCVD) [7]. In a previous study of as-deposited Fe/Sb_2Te_3 heterostructures [8], it has been revealed that only 50% of the Fe atoms at the interface (out of the 1 nm Fe in contact with Sb_2Te_3) were coordinated in a pure ferromagnetic phase. The rest of the Fe atoms at the interface have been found in paramagnetic configurations, and this is certainly detrimental in the view of exploiting charge-to-spin conversion phenomena in this system. As compared to results available for similar systems [9–12], a general bonding mechanism has been suggested, involving the Fe atoms and the chalcogen element in chalcogenide-based TIs.

Here, thanks to the use of interface-sensitive ^{57}Fe Conversion Electron Mössbauer Spectroscopy (CEMS), X-ray Diffraction and Reflectivity (XRD/XRR), Time-of-Flight Secondary Ions Mass Spectrometry (ToF-SIMS) and Vibrating Sample Magnetometry (VSM) analyses, we demonstrate that the proposed RTA methodology improves the TI structural quality and promotes the Fe/Sb_2Te_3 interface reconstruction, yielding the maximization of the ferromagnetic component in contact with the TI. The proposed method can be easily extended to different FM/TI systems, providing a general method to improve their interface quality.

2. Materials and Method

The deposition of polycrystalline Sb_2Te_3 thin films was carried out by MOCVD at room temperature (RT) on large-area (4'') SiO_2/Si substrates. Scanning Electron Microscopy (SEM) has previously evidenced the granular morphology of the deposited thin-film and the nominal thickness of about 30 nm [13]. The topological nature of this material has been proved through magneto-transport measurements [7]. The samples were subsequently transferred to a Pulsed Laser Deposition (PLD) chamber, where ^{54}Fe(10nm)/^{57}Fe(1nm) bilayers were grown in direct contact with Sb_2Te_3 at RT, similarly to what reported in Ref. [8]. In particular, the isotopically enriched (95%) 1 nm thick ^{57}Fe interlayer allowed to perform interface-sensitive Conversion Electron Mössbauer Spectroscopy (CEMS) analysis, in order to get atomic-scale structural, chemical and magnetic information about the interface [8, 14–16].

As a possible solution to optimize the quality of the Fe/Sb_2Te_3 interface, we analyzed different RTA strategies, in N_2 atmosphere. Initially, we employed the same recipe reported in Ref.[14], which was shown to improve the interface sharpness in several Fe/oxide heterostructures upon RTA of the whole Fe/oxide system. However, in the case of Fe/ Sb_2Te_3 system, this RTA process turned out to be detrimental for the interface quality [8]. The

alternative strategy of conducting the thermal annealing of Sb_2Te_3 only was applied, prior to Fe deposition. In particular, both RTA and slow-ramp thermal annealing were tried and the RTA turned out to be more efficient in improving the Sb_2Te_3 crystalline quality, with an identified maximum temperature of 200 °C (see *Supplementary Information Figure S1*).

Table 1 summarizes the stacks with the corresponding RTA treatments of Sb_2Te_3 applied before Fe deposition.

Table 1: List of the analyzed samples. The materials stack is the same for all the samples, while the Sb_2Te_3 is subjected to the different indicated RTA, prior to Fe deposition.

		RTA steps on Sb_2Te_3 (prior to Fe deposition)		
Sample	**Stack**	**Ramp up**	**Heating**	**Cooling Down**
SN	^{54}Fe(10nm) /^{57}Fe(1nm) /Sb_2Te_3/SiO_2	None	None	None
S150	^{54}Fe(10nm) /^{57}Fe(1nm) /Sb_2Te_3 /SiO_2	RT $\overset{10\,s}{\Longrightarrow}$ 150°C	150°C $\overset{10\,s}{\Longrightarrow}$ 150°C	150°C $\overset{250\,s}{\Longrightarrow}$ RT
S200	^{54}Fe(10nm) /^{57}Fe(1nm) /Sb_2Te_3/SiO_2	RT $\overset{10\,s}{\Longrightarrow}$ 200°C	200°C $\overset{10\,s}{\Longrightarrow}$ 200°C	200°C $\overset{250\,s}{\Longrightarrow}$ RT

CEMS analysis was carried out at RT in a constant-acceleration drive, with the sample mounted as an electrode in a parallel-plate avalanche detector filled with acetone gas. An α-Fe foil at RT was used for the CEMS velocity scale calibration and all the reported isomer shifts are relative to α-Fe.

The X-ray based structural-chemical analysis was performed by Grazing Incidence X-ray Diffraction (GIXRD) and X-Ray Reflectivity (XRR) measurements. GIXRD was performed using a Cu radiation with the K_α emission at λ = 1.54 Å and the patterns were collected with a position- sensitive gas detector (Inel CPS-120) [17]. Here, the rocking angle between the sample and the X-ray beam was fixed at ω=2°. XRR measurements allowed the determination of the thickness, the roughness and the electronic density (ρ_e) of each layer composing the sample. The XRR data were obtained using a commercial scintillator and modelled through a matrix formalism corrected by a Croce-Nevot factor. In particular, ρ_e is related to the measured critical vector Qc by the relation $\mathrm{Qc}\left(\text{Å}^{-1}\right) = 0.0375\sqrt{\rho_e(e^-/\text{Å}^3)}$ (for the Cu K_α emission).

Time of Flight Secondary Ion-Mass Spectrometry (ToF-SIMS) was employed to determine the elemental distribution in the heterostructures. We used an ION TOF IV instrument, using Cs+ ions with 500 eV for sputtering and Ga+ ions at E= 25 keV for the analysis. Further details concerning the materials and the analysis procedure can be found elsewhere [8].

Vibrating sample magnetometry (VSM) was carried out with a MicroSense EZ-9 instrument, which allowed to measure the magnetic hysteresis loops. VSM data provided the value of the saturation magnetization (M_s) and the direction of the easy axis of the magnetization at RT.

3. Results and Discussion

3.1. Structural and magnetic properties of the Fe/Sb_2Te_3 heterostructure

F*igure 1* shows the XRR analysis of the *SN* and *S200* samples, with the nominal layers thicknesses, electronic density and surface/interface roughness reported in *Table 2*, as obtained from the fit. For all samples, the data are interpreted by modelling the system with five layers. Clearly, the annealing up to T=200 °C did not affect the layers thickness, roughness and electronic density, with the stack being perfectly preserved (Table 2).

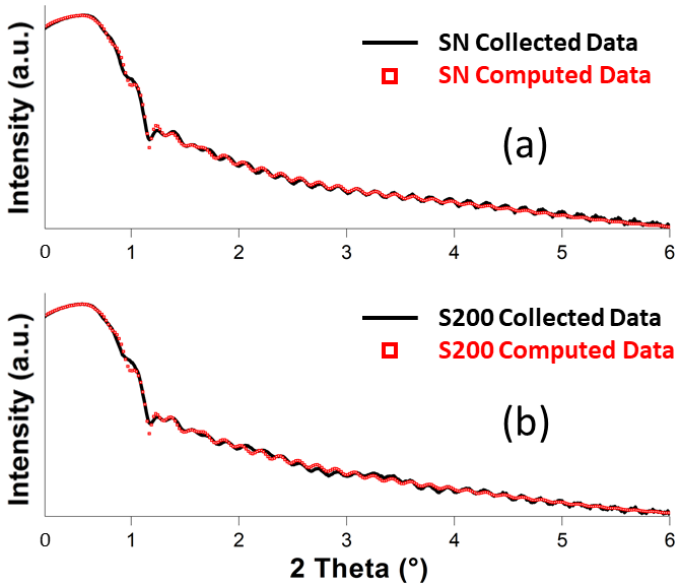

Figure 1: The collected XRR spectra (black solid line) and their computed models (red squares) for samples (a) SN and (b) S200.

Table 2: Values extracted from the fit of the XRR curves of the samples SN and S200. The error on thickness and roughness is ±0.1 nm and ± 0.05 $e^-/Å^3$ on electronic density.

Layers	**Thickness (nm)**	ρ_e ($e^-/Å^3$)	**Roughness (nm)**
	SN/S200	***SN/S200* [Nominal]**	***SN/S200***
FeO	2.8/3.1	1.7/1.7 [1.6]	2.4/2.3

Fe	6.2/6.3	2.2/2.2 [2.2]	2.4/2.0
Sb_2Te_3	27.7/27.7	1.5/1.5 [1.6]	2.3/2.1
Sb_2O_3	1.6/1.5	1.4/1.5 [1.5]	0.2/0.1
SiO_2	50.0/50.3	0.8/0.8 [0.8]	0.4/0.4

On the other hand, the crystal quality of the Fe and Sb_2Te_3 layers was largely affected by the thermal annealing. *Figure 2* shows the GIXRD patterns for all samples (*Table 1*), and the data are compared to the powder diffraction pattern of cubic α-Fe (black line) and Sb_2Te_3 (pink line). The latter is characterized by a rhombohedral crystal structure belonging to the R-3m space group. In agreement with previous studies [18], the crystalline grains of the Sb_2Te_3 substrate showed an out-of-plane [OOP] orientation along the [00ℓ] direction. Through X-ray measurements conducted in Bragg-Brentano geometry, we correlated the higher intensity of the (003), (006) and (009) peaks present in the GIXRD patterns, as compared to the powder, with the presence of such [00ℓ] OOP orientation [8]. From *Figure 2*, we observed that the peaks relative to the [00ℓ] direction become more intense and sharper as a function of the RTA temperature, as highlighted in *Figure 2(d).* This corresponds to an improvement of the Sb_2Te_3 layer crystallization and it is a clear indication that the amorphous fraction of the as-deposited Sb_2Te_3 compound becomes crystalline and oriented along the [00ℓ] direction. Moreover, the

overall enhanced crystalline quality of the Sb_2Te_3 layer is reflected in the increased intensity of the peaks other than those related to the 00ℓ reflections, as clear at $2\Theta \sim 38°$ in *Figure 2(a-c)*.

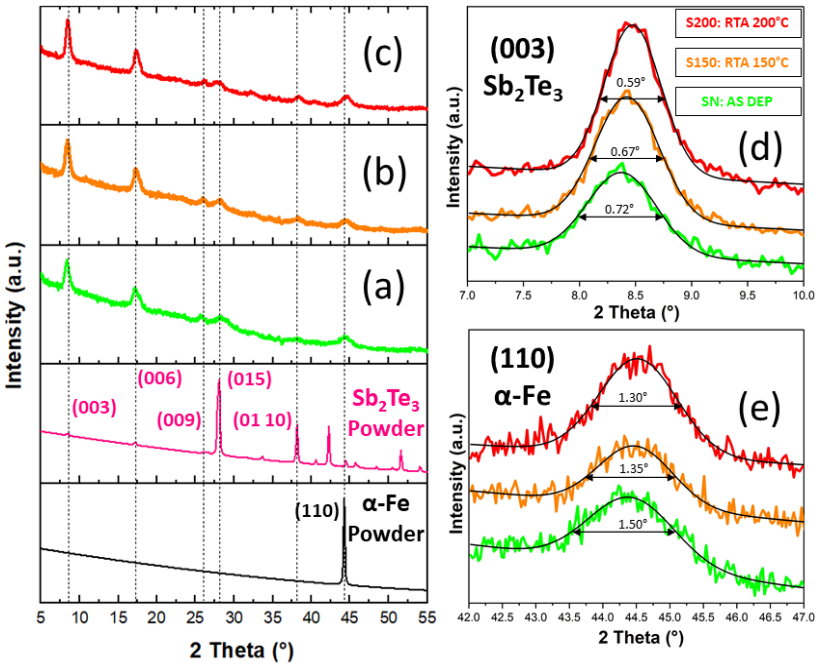

Figure 2: GIXRD pattern of samples (a) SN, (b) S150, and (c) S200. For the Sb_2Te_3 and α-Fe powder diffraction patterns please refer to ICSD Code:2084 and ICSD Code:53802, respectively. Panels (d) and (e) represent the evolution of the Sb_2Te_3 (003) and Fe (110) reflections after thermal annealing, respectively.

Unexpectedly, the improved crystalline quality of Sb_2Te_3 as a consequence of the RTA, also affected the crystalline quality of the Fe layer later deposited on top. *Figure 2(e)* depicts the evolution of the peak positioned around $2\Theta \sim 44°$ corresponding to the Fe (110) planes reflection of the α-Fe crystalline phase, which remarks two aspects of interest. First, the peak shrinks, with a full half-width maximum (FHWM), going from 1.50° in *SN* to 1.30-1.35° in *S150* and *S200*, respectively. Secondly, the peak intensity clearly increases, which is a further demonstration that the RTA of the Sb_2Te_3 film induced an enhanced crystallization of the Fe layer deposited on top.

Figure 3 shows the hysteresis loops acquired by VSM at RT for the samples *SN* (blue curve) and *S200* (red curve), with the external magnetic field applied in the film plane. The easy axis of the magnetization lies in the plane (IP) of the Fe layer, while the OOP direction is a hard axis (from the comparison of the red and green lines in the inset of Figure 3), in agreement with CEMS and, as expected, due to the magnetic shape anisotropy contribution.

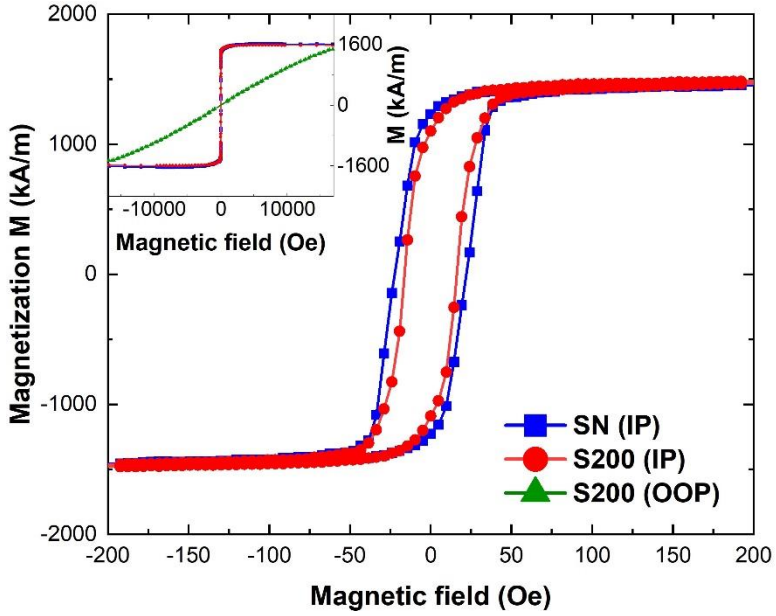

Figure 3: In-plane magnetic hysteresis loops for the samples SN (blue curve) and S200 (red curve) at relatively low fields. The inset shows the magnetic response up to saturation. The green curve shows the out-of-plane loop for sample S200.

The saturation magnetization (M_s) resulted to be around 1600 kA/m (or emu/cm^3) for the two samples (within the error bar of about 5%). The value of M_s, very similar to that reported for bulk α-Fe (1700 kA/m), evidenced the good magnetic quality of the films, also considering the presence of a FeO_x layer at the surface (*Table 2*) due to the absence of any capping layer. The squareness of the hysteresis loops, evaluated as the ratio between the magnetization at remanence and at saturation, was around 70% for both the samples, which is compatible with the polycrystalline structure of the film. The coercive field reduced from 22 Oe in *SN* to 16 Oe in *S200*. We attributed this change to the observed enhanced crystalline degree of Fe (*Figure 2(e)*), which possibly induces the formation of larger Fe grains and magnetic domains in case of RTA of the chalcogenide film. Note that, in general, the possibility to reduce the coercive field of a FM film in contact with a thermally treated 3D-TI could be beneficial in devices, reducing the energy required to switch the FM magnetization through a spin-transfer torque effect at the FM/TI interface.

3.2. Effect of the Sb_2Te_3 RTA on the chemical, structural and magnetic properties of the Fe/Sb_2Te_3 buried interface

ToF-SIMS was performed on samples *SN* and *S200* and reported in *Figure 4*. The best sensitivity for the Fe atoms detection was reached by tracking the ^{54}FeO (orange line) and ^{57}FeO

(green line) profiles across the heterostructures. Observing the evolution of the curves, the stacking order of the layers is respected. Following the ^{54}FeO orange line as a function of the

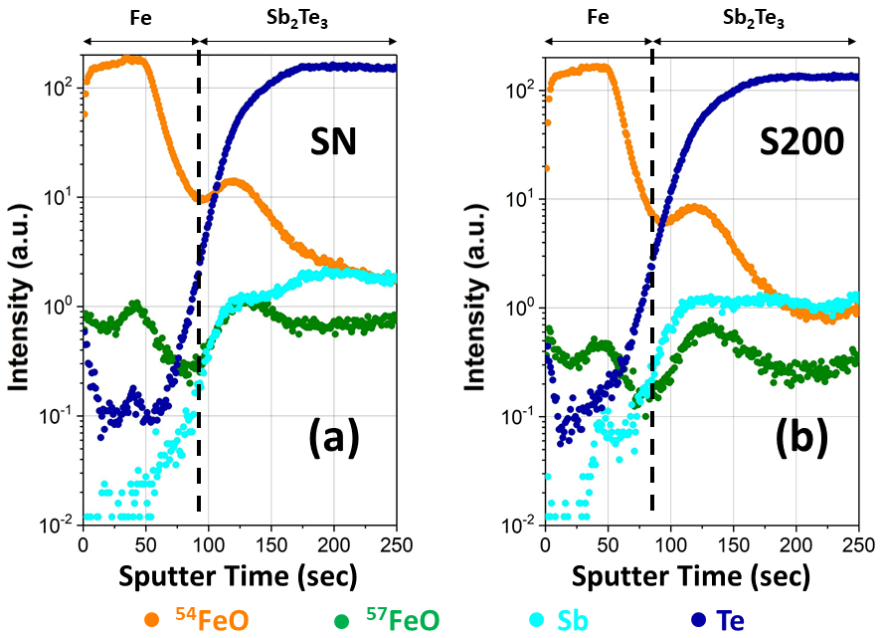

Figure 3: ToF-SIMS measurements of samples SN and S200. A qualitative comparison between (a) and (b) showed *that few differences are present in SN and S200, which is a proof of the interface stability following the RTA.*

sputtering time, it can be noticed that the ^{54}Fe layer is the first one on top of the stack, but a more interesting feature is connected to the ^{57}Fe green lines: following a ~50 sec sputtering time, these curves showed a relative maximum in both *SN* and *S200*, which is related to the presence of the ^{54}Fe/^{57}Fe interface. By comparing the evolution of the Te and Sb signals before and after the annealing treatment, it could be concluded that no intermixing occurred between the Fe layer and the Sb_2Te_3 substrate. Moreover, the ToF-SIMS analysis demonstrated that the ^{57}Fe tracer-layer is confined between the ^{54}Fe and Sb_2Te_3 layers in both *SN* and *S200*, thus allowing to attribute the chemical, structural and magnetic characterization by CEMS (described below) exclusively to the buried Fe/Sb_2Te_3 interface.

Figure 5(a) shows the ^{57}Fe-CEMS analysis on samples *SN*, *S150* and *S200*. All the spectra could be analyzed in terms of four components: α-Fe, DIST, DOUB-1 and DOUB-2, as in Ref. [8]. *Table 3* summarizes the fitting parameters, where δ indicates the isomer shift, ΔE_Q the quadrupole splitting, $\langle B_{hf} \rangle$ the average hyperfine magnetic field, $\langle \Gamma \rangle$ the average line width and A_{25} the ratio between lines (1,6) and (2,5) of the magnetically-split components. *Figure 4(b)* shows the evolution of the relative spectral areas for each fitting component, as obtained by assuming the Debye-Waller factor equal to 1 for all of them. The fitting strategy was to fix the same values of the hyperfine parameters for all the fitted components in *SN*, *S150* and *S200*, leaving only the relative areas (*Figure 5(b)*) and the $\langle B_{hf} \rangle$ of the DIST component (*Table 3*) free to vary.

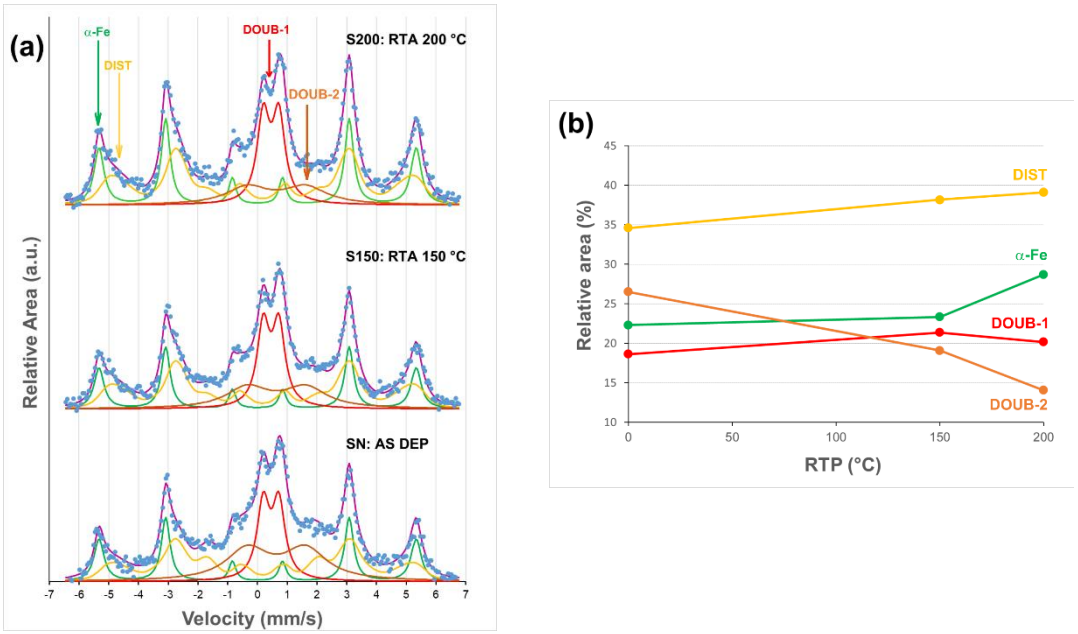

Figure 4: (a) CEMS measurements of samples SN, S150 and S200. The blue points are the experimental data and the superimposed purple solid line is the simulated curve, as obtained by the sum of the indicated fitting components: α-Fe, DIST, DOUB-1, and DOUB-2; (b) corresponding RTA-dependence of the relative areas of the four fitting components.

Table 3: CEMS parameters extracted from the fit of the data shown in Figure 5(a). Where the experimental error is not indicated, this means the parameter was fixed during the fitting procedure.

	Parameters	α -Fe	DIST	DOUB-1	DOUB-2
	δ (mm/s)	0,0	0,17(1)	0,46(1)	0,64(2)
	ΔE_Q (mm/s)	0,0	0,0	0,52(1)	1,95(3)
SN	$< B_{hf} >$(T)	33,02(3)	26,58(3)	-	-
S150	$< B_{hf} >$(T)	33,02(3)	28,57(3)	-	-
S200	$< B_{hf} >$(T)	33,02(3)	28,82(3)	-	-
	$< \Gamma >$ (mm/s)	0.35(1)	0.5	0.5	1,72(4)
	A_{25}	4	4	-	-

The α-Fe contribution is due to unreacted ^{57}Fe atoms, which maintained unperturbed their local environment. DIST is a distribution of broadened magnetically-split sextets, and it was attributed to under-coordinated ^{57}Fe atoms in direct contact with the Sb_2Te_3 layer. When compared to α-Fe, DIST is characterized by a lower $<B_{hf}>$ and an enhanced isomer shift (*Table 3*), thus pointing to the occurrence of a hybridization between the Fe atoms and Sb_2Te_3, leading to a lower electronic density around Fe atoms at the interface [8]. The doublets DOUB-1 and DOUB-2 were associated with two paramagnetic phases. DOUB-1 was attributed to FeTe, while DOUB-2 was attributed either to the presence of FeO_x or $FeSb_2$ [8,19]. The A_{25} value associated with this ferromagnetic portion showed that the magnetization is always directed in the film plane, in accordance with the VSM data (*Figure 3*). The increase of $<B_{hf}>$ for the DIST component in *S200*, when compared to *SN* (*Table 3*), further supported the hypothesis that, upon the RTA of Sb_2Te_3, the Fe atoms at the Fe/Sb_2Te_3 interface tend to reorganize toward pure α-Fe. As a matter of fact, we detected an ~8% increase of the $<B_{hf}>$ for the DIST component when moving from *SN* to *S200* (Table 3). This reflects an overall increase of the magnetic moment at the Fe/Sb_2Te_3 interface, as originated from the higher crystallinity of the corresponding underlying Sb_2Te_3 layer.

Figure 5(b) summarizes the main effect of the RTA of Sb_2Te_3, on the chemical, structural and magnetic configuration of the interfacial Fe atoms, where a gradual increase of the magnetic (α-Fe + DIST) fraction (of ~11%) was observed. Correspondingly, a gradual lowering of the DOUB-2 fraction (from ~27% to ~14%) was observed (error bars in the spectral areas is around 2%). Based on the present findings, we answered the so-far open question about the attribution of the DOUB-2 component, which, according to its gradual lowering upon the Sb_2Te_3 RTA, was attributed to FeO_x. The proposed RTA favored the

formation of a sharper and structurally purer Fe/Sb_2Te_3 interface. The presence of O at the Sb_2Te_3 surface is unavoidable, as far as Sb_2Te_3 is not capped before being transferred to the PLD system, to deposit Fe on top. This is exactly why our results are of importance, demonstrating that the Sb_2Te_3 crystalline quality and chemical purity can be almost-fully restored with an appropriate mild thermal processing, thus avoiding the need to develop a dedicated process to cap the TI, and to later fully un-cap it, prior to the FM deposition.

The combination of CEMS, GIXRD and VSM, clearly confirmed the scenario where the improved crystalline quality obtained in Sb_2Te_3 (*Figure 2(c)*), through the proposed mild thermal annealing, is efficient in improving both the Fe crystalline quality (*Figure 2(d)*), and the buried Fe/Sb_2Te_3 interface chemical, structural and magnetic quality, as observed at the most-atomic-scale (*Figure 5*).

In order to provide an overview about the chemical-structural differences among the samples studied in this work and those previously reported [8], the corresponding GIXRD and CEMS data were compared (*Supplementary Information Section 2*). The observed differences were attributed to the different crystalline quality of the as-deposited Sb_2Te_3 layer in the two cases, which affected the chemical composition at the Fe/Sb_2Te_3 interface. In particular, the *SN* sample studied in the present work is characterized by a higher crystallinity, which was correlated with the higher fraction of the magnetic DIST component of the CEMS data at the expense of the paramagnetic fraction, when compared to the as-deposited case reported in Ref.[8].

3.3. Formation of FeTe at the Fe/Sb_2Te_3 interface

A fundamental aspect characterizing the Fe/Sb_2Te_3 interface emerged when focusing on DOUB-1 detected by CEMS, which was attributed to the formation of FeTe at the interface. While the effect of the RTA on the buried Fe/Sb_2Te_3 interface is a clear change of the spectral area fractions of α-Fe, DIST and DOUB-2, there is a negligible change in the FeTe fraction (*Figure 5(b)*). This result nicely supported previous insights about a strong tendency of Fe to bond with the chalcogen atoms of chalcogenides-TI [8,9]. Moreover, the presented RTA experiments marked an upper limit for the thermal treatment that preserves the FeTe before being affected by the Sb_2Te + 2Te dissociation, as observed for T> 200 °C (*Supplementary Information Figure S1*).

The potential role that this small fraction of interfacial FeTe can play in a charge-to-spin conversion in Fe/Sb_2Te_3 is difficult to foresee and may be detrimental. On the other hand, at the particular conditions, the stabilization of the FeTe phase may give rise to superconductivity, making the Fe/FeTe/Sb_2Te_3 system of potential interest for investigating the exotic interplay between superconductivity, topology and magnetism [19–21]. This motivated us to provide a thermodynamic picture of what happens at the Fe/Sb_2Te_3 interface, as described in the following.

The favorable FeTe thermodynamic stability is supported by the following arguments previously reported by *I. Vobornik et al.* [11] and *L.A. Walsh et al.* [10] for several FM/TI compounds. The equation $\Delta G^0 = \Delta H^0 - T\Delta S^0$ is the standard-state Gibbs free energy variation as a function of the changes in the enthalpy H and entropy S in the system ($\Delta G^0\ (H, S)$), at the absolute temperature T (here fixed at T = 298 K). In Ref. [11] the authors have investigated the possible reactions which could take place at the Fe/Bi_2Te_3 interface using a standard thermodynamic tabulation [22], highlighting the natural tendency of Fe atoms to react with Bi_2Te_3 forming $FeTe_{0.9}$ ($\Delta G^0_{FeTe_{0.9}}$ spans from $-4.5\ to\ 0.5\ \frac{kJ}{mol \cdot Fe}$) and $FeTe_2$ ($\Delta G^0_{FeTe_2}$ spans from $-17.5\ to\ -6.6\ \frac{kJ}{mol \cdot Fe}$) compounds. Similarly, in Ref.[10] the Fe/Bi_2Se_3 has been investigated in terms of thermodynamic properties, pointing out, also in this case, the high reactivity between Fe and Se atoms. In particular, here the authors have identified as the most favorable reaction the formation of Fe_3Se_4 ($\Delta G^0_{Fe_3Se_4} = -244.0\ \frac{kJ}{mol \cdot Fe}$) and, through Angle-Resolved X-Ray Photoemission Spectroscopy, they have showed that $FeSe_x$ compounds are more surface-localized, proving the Fe and Se interdiffusion at the Fe/Bi_2Se_3 interface. Here, using the data reported in Ref. [23], the ΔG^0 values for the $FeSe_{0.961}$ and $FeSe_2$ formation (not shown in Ref. [10]) were calculated and reported in *Section 3* of the *Supplementary Information*.

In order to make a comparison with the above studies, we performed similar thermodynamic calculations for our Fe-Sb_2Te_3 systems. The possible chemical reactions we identified are those indicated with *Equation (1-4)*.

$$3Fe + 0.9Sb_2Te_3 \rightarrow 3FeTe_{0.9} + 1.8\,Sb \qquad \Delta G^0_{FeTe_{0.9}} = -8.09\ \frac{kJ}{mol \cdot Fe} \qquad [1]$$

$$Fe + 0.9Sb_2Te_3 \rightarrow FeTe_{0.9} + 1.8\,SbTe \qquad \Delta G^0_{FeTe_{0.9}} = 100\ \frac{kJ}{mol \cdot Fe} \qquad [2]$$

$$3Fe + 2Sb_2Te_3 \rightarrow 3FeTe_2 + 4\,Sb \quad \Delta G^0_{FeTe_2} = -34.8\ \frac{kJ}{mol \cdot Fe} \qquad [3]$$

$$Fe + 2Sb_2Te_3 \rightarrow FeTe_2 + 4\,SbTe \quad \Delta G^0_{FeTe_2} = 661.3\frac{kJ}{mol \cdot Fe} \qquad [4]$$

In these calculations, other possibilities connected to the dissociation of Sb_2Te_3 in $FeTe_x$ + Sb_2Te were not considered since, at least to our knowledge, no thermodynamic data are

available for the Sb_2Te binary compound. As it is evident, the most favored reactions between Fe and Sb_2Te_3 involve the formation of $FeTe_{0.9}$ and $FeTe_2$ accompanied by the dissociation of the elemental Sb. On the contrary, the formation of the SbTe compound is highly unfavorable.

4. Conclusion

We performed a comprehensive chemical, structural, and magnetic study of the Fe/Sb_2Te_3 heterostructure as a function of RTA of Sb_2Te_3 up to 200 °C, prior to Fe deposition. The combination of XRR, GIXRD, VSM, ToF-SIMS, and CEMS analyses demonstrated clear correlation between the enhanced crystalline quality of Sb_2Te_3 layers and the improved chemical, structural and magnetic properties of the buried Fe/Sb_2Te_3 interface reconstruction, which also partly affected the macroscopic magnetic properties of the 10 nm-Fe layer by reducing the coercive field. In particular, XRR and ToF-SIMS demonstrated that the Fe/Sb_2Te_3 interface is chemically stable up to 200 °C, with a preserved stack integrity and no detectable differences in terms of intermixing. Following interface-sensitive CEMS analysis (being confined to the first 1 nm ^{57}Fe marker layer in contact with Sb_2Te_3), we further investigated the atomic-scale rearrangement to which the Fe atoms are subjected. We observed an overall enhanced quality of the interface upon RTA of Sb_2Te_3, as demonstrated by the increase (of about 11%) of the overall magnetic fraction following RTA at 200 °C, that was attributed to the lowering of the FeO_x paramagnetic fraction at the interface. Interestingly, the ~20% fraction of FeTe at the interface was almost unaffected by the RTA, thus strongly supporting that there is a thermodynamic driving force favoring the formation of such a compound at the interface, as confirmed by theoretical calculations. By comparing our results with the data available in the literature for similar systems, we suggested the tendency of Fe to bond with the chalcogen atom of a chalcogenide-based TI to be a general phenomenon.

In principle, the proposed RTA process can be extended to other FM/TI systems, thus providing a tool for optimizing the interface quality without the use of TI's capping interlayers. At the same time, the conducted atomic-scale analysis of the interface properties, revealed the importance of controlling the chemical reactions taking place at the Fe/TI interface during the Fe deposition, especially for monitoring the formation of paramagnetic compounds, potentially detrimental for charge-to-spin conversions applications.

Moreover, the appropriate engineering of ultrathin FeTe-based superconductors in the $Fe/FeTe/Sb_2Te_3$ heterostructures, may open strategies to exploit the interplay between topology and superconductivity to realize the elusive Majorana fermion, as previously proposed [19].

Acknowledgments

We acknowledge the Horizon 2020 project SKYTOP "*Skyrmion-Topological Insulator and Weyl Semimetal Technology*" (FETPROACT-2018-01, n. 824123). C.R. acknowledges the project ECOS by Fondazione Cariplo and Regione Lombardia, grant no. 2017-1622, and the PRIN project TWEET funded by MIUR (No. 2017YCTB59). Part of this work was performed using the equipment of MIPT Center of Shared Facilities.

Bibliography

[1] J. Sinova, S. O. Valenzuela, J. Wunderlich, C. H. Back, T. Jungwirth, *Reviews of Modern Physics* **2015**, *87*, 1213.
[2] F. Hellman, A. Hoffmann, Y. Tserkovnyak, G. S. D. Beach, E. E. Fullerton, C. Leighton, A. H. MacDonald, D. C. Ralph, D. A. Arena, H. A. Dürr, P. Fischer, J. Grollier, J. P. Heremans, T. Jungwirth, A. V. Kimel, B. Koopmans, I. N. Krivorotov, S. J. May, A. K. Petford-Long, J. M. Rondinelli, N. Samarth, I. K. Schuller, A. N. Slavin, M. D. Stiles, O. Tchernyshyov, A. Thiaville, B. L. Zink, *Reviews of Modern Physics* **2017**, *89*, DOI 10.1103/RevModPhys.89.025006.
[3] A. Soumyanarayanan, N. Reyren, A. Fert, C. Panagopoulos, *Nature* **2016**, *539*, 509.
[4] Y. Wang, D. Zhu, Y. Wu, Y. Yang, J. Yu, R. Ramaswamy, R. Mishra, S. Shi, M. Elyasi, K.-L. Teo, Y. Wu, H. Yang, *Nature Communications* **2017**, *8*, DOI 10.1038/s41467-017-01583-4.
[5] Y. Wang, R. Ramaswamy, H. Yang, *J. Phys. D: Appl. Phys.* **2018**, *51*, 273002.
[6] A. R. Mellnik, J. S. Lee, A. Richardella, J. L. Grab, P. J. Mintun, M. H. Fischer, A. Vaezi, A. Manchon, E.-A. Kim, N. Samarth, D. C. Ralph, *Nature* **2014**, *511*, 449.
[7] R. Cecchini, R. Mantovan, C. Wiemer, L. Nasi, L. Lazzarini, M. Longo, *physica status solidi (RRL) - Rapid Research Letters* **2018**, *12*, 1800155.
[8] E. Longo, C. Wiemer, R. Cecchini, M. Longo, A. Lamperti, A. Khanas, A. Zenkevich, M. Fanciulli, R. Mantovan, *Journal of Magnetism and Magnetic Materials* **2019**, *474*, 632.
[9] S. Majumder, K. Jarvis, S. K. Banerjee, K. L. Kavanagh, *Journal of Vacuum Science & Technology B, Nanotechnology and Microelectronics: Materials, Processing, Measurement, and Phenomena* **2017**, *35*, 04F105.
[10] L. A. Walsh, C. M. Smyth, A. T. Barton, Q. Wang, Z. Che, R. Yue, J. Kim, M. J. Kim, R. M. Wallace, C. L. Hinkle, *The Journal of Physical Chemistry C* **2017**, *121*, 23551.
[11] I. Vobornik, G. Panaccione, J. Fujii, Z.-H. Zhu, F. Offi, B. R. Salles, F. Borgatti, P. Torelli, J. P. Rueff, D. Ceolin, A. Artioli, M. Unnikrishnan, G. Levy, M. Marangolo, M. Eddrief, D. Krizmancic, H. Ji, A. Damascelli, G. van der Laan, R. G. Egdell, R. J. Cava, *The Journal of Physical Chemistry C* **2014**, *118*, 12333.
[12] C. Rinaldi, S. Varotto, M. Asa, J. Sławińska, J. Fujii, G. Vinai, S. Cecchi, D. Di Sante, R. Calarco, I. Vobornik, G. Panaccione, S. Picozzi, R. Bertacco, *Nano Lett.* **2018**, *18*, 2751.

[13] M. Longo, S. Cecchi, S. Selmo, M. Fanciulli, C. Wiemer, J.-L. Battaglia, A. Saci, A. Kusiak, in *2015 1st Workshop on Nanotechnology in Instrumentation and Measurement (NANOFIM)*, IEEE, Lecce, **2015**, pp. 150–154.
[14] R. Mantovan, C. Wiemer, A. Lamperti, M. Georgieva, M. Fanciulli, A. Goikhman, N. Barantsev, Yu. Lebedinskii, A. Zenkevich, *Hyperfine Interact.* **2009,** 191, 41.
[15] A. Zenkevich, R. Mantovan, M. Fanciulli, M. Minnekaev, Yu. Matveyev, Yu. Lebedinskii, S. Thiess, W. Drube, *Applied Physics Letters* **2011**, *99*, 182905.
[16] R. Mantovan, C. Wiemer, A. Zenkevich, M. Fanciulli *Hyperfine Interact.* **2006**, 169, 1349.
[17] C. Wiemer, S. Ferrari, M. Fanciulli, G. Pavia, L. Lutterotti, *Thin Solid Films* **2004**, *450*, 134.
[18] E. Longo, R. Mantovan, R. Cecchini, M. D. Overbeek, M. Longo, G. Trevisi, L. Lazzarini, G. Tallarida, M. Fanciulli, C. H. Winter, C. Wiemer, *Nano Res.* **2020**, *13*, 570.
[19] Y. Mizuguchi, F. Tomioka, S. Tsuda, T. Yamaguchi, Y. Takano, *Physica C: Superconductivity* **2009**, *469*, 1027.
[20] S. Manna, A. Kamlapure, L. Cornils, T. Hänke, E. M. J. Hedegaard, M. Bremholm, B. B. Iversen, Ph. Hofmann, J. Wiebe, R. Wiesendanger, *Nat Commun* **2017**, *8*, 14074.
[21] Q. L. He, H. Liu, M. He, Y. H. Lai, H. He, G. Wang, K. T. Law, R. Lortz, J. Wang, I. K. Sou, *Nat Commun* **2014**, *5*, 4247.
[22] M. Binnewies, E. Milke, Eds. , in *Thermochemical Data of Elements and Compounds*, Wiley-VCH Verlag GmbH, Weinheim, Germany, **2002**, pp. i–iv.